Quantifying the processes of accelerated wintertime Tibetan Plateau warming: External forcing versus local feedbacks

Mengchu Zhao
Nanjing University
Xiu-Qun Yang (xqyang@nju.edu.cn)
Nanjing University
Lingfeng Tao
Nanjing University

Research Article

Keywords: Tibetan Plateau, accelerated warming, external forcing, snow-albedo feedback, moisture process feedback

Posted Date: October 21st, 2022

DOI: https://doi.org/10.21203/rs.3.rs-2170533/v1

Quantifying the processes of accelerated wintertime Tibetan Plateau warming: External forcing versus local feedbacks

Mengchu Zhao[a], Xiu-Qun Yang[a, b], Lingfeng Tao[a]

[a] *CMA-NJU Joint Laboratory for Climate Prediction Studies, School of Atmospheric Sciences, Nanjing University, Nanjing 210023, China*

[b] *Southern Marine Science and Engineering Guangdong Laboratory (Zhuhai), Zhuhai 519082, China*

Corresponding author address: Dr. Xiu-Qun Yang, xqyang@nju.edu.cn,

School of Atmospheric Sciences

Nanjing University, Nanjing 210023, China

ABSTRACT

The Tibetan Plateau (TP) has experienced an accelerated wintertime warming in recent decades under global warming, but consensus on its causes has not yet been reached. This study quantifies the processes of the warming through analyzing surface temperature budget and surface energy balance. It is found that increased diabatic heating (71%) and warm advection (29%) by an anomalous anticyclone southeast of TP are two primary processes determining the surface air warming. The former is caused by a significant increase of the TP skin temperature which warms the near surface atmosphere through increasing upward surface sensible heat flux. The land surface warming is attributed to increased absorbed radiation fluxes in which three processes are identified to be major contributors. While external forcing which is primarily due to increased anthropogenic emissions of greenhouse gases contributes to the warming by 24% through increasing downward longwave radiation, two types of local positive feedbacks which are triggered by the land surface warming are found to contribute to most of the warming. One is the snow-albedo feedback which accounts for 47% of the surface warming by increasing surface absorption of incident solar radiation. The other is the moisture process feedback which accounts for 29% of the surface warming. The surface warming which works with increased soil moisture due to increased precipitation in the preceding seasons tends to promote surface evaporation and moisten the atmosphere aloft over the eastern TP, which, in turn, tends to increase downward longwave radiation and cause a further surface warming.

Keywords: Tibetan Plateau, accelerated warming, external forcing, snow-albedo feedback, moisture process feedback

1. Introduction

The Tibetan Plateau (TP), with an average elevation of over 4000m and an area of approximately 2.5×10^6 km^2, referred to as “the third pole” or “Asian water tower”, is the highest and most spatially extensive highland in the world (Niu et al. 2004; Yao et al. 2019a; Zhao and Zhou 2020). Climate over TP is highly sensitive to global climate change due to its unique landforms and geographical location (Wu et al. 2015; Wu et al. 2022; Yao et al. 2012; Yao et al. 2015). In the context of global warming, evident climate changes emerge in TP including glacier shrinkage, lake expansion, atmospheric moistening and near surface accelerating warming (Meng et al. 2019; Wang et al. 2013; Wu et al. 2014; Yan et al. 2020a; Yang et al. 2011; Yao et al. 2019b). Among them the near surface accelerated warming over TP which is also regarded as the “TP amplification” is one of the most significant characteristics of climate changes over TP (Group 2015; Wu et al. 2020; You et al. 2021; You et al. 2017).

The surface air temperature (SAT) warming over TP starts in the early 1950s, much earlier than over the Northern Hemisphere which starts in the mid-1970s (Liu and Chen 2000; Niu et al. 2004). Since the beginning of the 1980s, there is a stronger warming rate over TP exceeding that of Northern Hemisphere or global means over the same period (Duan and Xiao 2015; Gao et al. 2015; Yao et al. 2019b). The strongest warming trend occurred in winter, with a rate of twice as the annual mean (Cai et al. 2017; Liu and Chen 2000; You et al. 2017). Several potential mechanisms have been put forward for the wintertime accelerated warming of TP, including changes in anthropogenic emissions of greenhouse gases (GHGs), atmospheric heat transport, local surface-based feedback processes, and cloud radiative forcing (Duan et al. 2022; Duan et al. 2006; Duan and Xiao 2015; Qu et al. 2019; Yan et al. 2016).

In terms of external forcing out of TP, the increased emissions of GHGs are recognized as the primary driver of accelerated TP warming in the winter half year through enhancing both downward solar and thermal radiation fluxes reaching the surface (Duan et al. 2006; Wu et al. 2020; Yan et al. 2016; Yao et al. 2015). Moreover, the TP near surface air temperature change can be attributed to long-term trend of atmospheric circulation. The decline of sea ice concentration over the Barents-Kara Sea tends to excite a Rossby wavetrain propagating southeastward to TP, which increases warm advection transport and enhances wintertime TP warming (Duan et al. 2022). The processes of atmospheric circulation anomalies induced by global warming are complex, because the long-term trends of the circulation anomalies arise from both external forcing and internal climate variability. Some explanations of the circulation anomalies around TP exists. For instance, You et al. (2010) proposed that the weakening of southern extent of the winter monsoon prevents TP from incursions of cold air. Changes of atmospheric circulation are conducive to the TP warming since the 1980s, but how the circulation trend pattern can be formed is still under debate (Blackport and Screen 2020; Smith et al. 2022; Sun et al. 2022; Wang et al. 2022).

Several studies have found that local radiative processes may contribute to ground surface temperature (GST) warming on TP through changing absorption of radiation fluxes by surface. Snow-albedo feedback could be one of the most important feedbacks for the surface warming. Observations exhibit declines of the snow depth and the number of snow-cover days over TP (Xu et al. 2017). The decrease of snow cover due to positive temperature anomalies reduce the surface albedo and more shortwave radiation are absorbed by surface, thus increasing GST rapidly (Ghatak et al. 2014; Pepin et al. 2019; Rangwala et al. 2013; You et al. 2017; Zhang et al. 2021). In terms of cloud radiative forcing, a decline of daytime cloud cover and an increase of nocturnal cloud cover are observed over TP, which favor increases of sunshine duration and downward longwave radiation (DLR) and partly contribute to the accelerated warming over TP (Duan and Wu 2006; Duan and Xiao 2015). Besides, while water vapor is an important greenhouse gas to modulate downward radiation, the sensitivity of DLR to changes in atmospheric water vapor is large in a climatologically dry condition according to a power function between clear sky DLR and specific humidity (Rangwala et al. 2009; Ruckstuhl et al. 2007). The wintertime TP is in accordance with such a cold-dry circumstance, thus increases in water vapor appear to be part of the reason for surface warming in theory. However, it is still unclear how water vapor can change and affect the surface warming over TP in winter.

Given the importance of radiative processes in modulating the TP surface temperature, it is necessary to examine the surface energy balance in order to explain the observed GST change (Clark et al. 2021; Gao et al. 2019; Xie et al. 2022). Since SAT generally varies in phase with GST, many previous studies used GST in replace of SAT to explicate the TP near surface air warming from the perspective of surface-based radiative process change, without considering the effect of atmospheric heat transport. Those studies investigating the role of atmospheric circulation change in the TP warming did not take into consideration the thermodynamic coupling between the surface and the atmosphere, as well as the importance of surface radiation processes changes in the surface air warming. The obfuscation of previous studies in using GST and SAT prevents us from realizing the contribution of local and external processes to the accelerated TP warming. Actually, the SAT and GST changes are governed by different equations. The SAT change is governed by the thermodynamic equation, while the GST change can be determined by the surface energy balance relation. It can be hypothesized that the ground surface warming which is driven by changes in surface radiative processes tends to enlarge temperature difference between land surface and air, and then to result in a rapid increase in SAT via increasing upward sensible heat flux, which manifests a positive diabatic heating anomaly at near surface level. Such a thermodynamic coupling is proposed to be critical in the wintertime Arctic amplification (Xie et al. 2022), which is emphasized in this study to quantify the processes of accelerated wintertime TP warming.

In this study, the long-term trends of changes in both SAT and GST are systematically investigated with observational and reanalysis datasets, and the processes responsible for the accelerated wintertime TP warming are identified by diagnosing the surface energy balance and surface air temperature budget, in which the relative contributions of external forcing and local feedback to the accelerated TP warming are quantified. Considering the uncertainties of reanalysis datasets in long-term trend of surface air temperature over TP (Wang et al. 2020; Yan et al. 2020b; You et al. 2013), six reanalysis datasets are compared with in-situ records for the surface air temperature. The rest of the paper is organized as follows. Datasets and methods used in this study are described in Section 2. Observed trend of wintertime SAT change over TP and evaluation of reanalysis datasets used are documented in Section 3. Section 4 diagnoses causes of the warming trend in SAT by using thermodynamic equation. Radiative processes responsible for the warming trend in GST are identified with surface energy balance equation in section 5. Final section is devoted to conclusions and discussion.

2. Data and methods

a. data

Datasets of monthly SAT at 2m and snow depth from in situ observations for TP region are provided by China Meteorological Administration (CMA), in which 80 stations are selected (Duan et al. 2018). The locations of those stations are shown in Fig. 1d, with 77 stations in the central-eastern TP and 3 stations to the west of 85°E. Details of the stations including station name, ID, latitude and longitude can be seen in Duan et al. (2018). To calculate the station-averaged SAT trend, the stations are allocated into 1°×1° rectilinear grids before averaging for reducing the statistical errors caused by uneven distribution of stations following Zhou and Wang (2017). Daily outputs of six reanalysis datasets provided by five organizations are utilized in this study, with detailed information listed in Table 1. These reanalysis datasets include the fifth generation ECMWF reanalysis (ERA-5) (Hersbach et al. 2020), the ECMWF interim reanalysis (ERA-Interim, hereafter ERA-I) (Dee et al. 2011), the CMA reanalysis project (CRA-40) (Zhao et al. 2019), the Japanese 55-year Reanalysis (JRA-55) (Ebita et al. 2011), the Modern-Era Retrospective Analysis for Research and Applications, version 2 (MERRA-2), and the NCEP–DOE Reanalysis 2 (NCEP-2) (Kanamitsu et al. 2002). CRA-40 was launched in 2014, which assimilates multiple data from conventional observations and satellite instruments, especially over East Asia (Liu et al. 2017; Zhao et al. 2019). In the subsequent comparative assessment in Section 3, the winter-averaged SATs at 2m over TP taken from six reanalyses are interpolated into horizontal grids the same as that used in the observation. The time span in this study is from January 1980 to December 2020. The wintertime is defined as December of the preceding year and January and February of the current year.

b. methods

In order to understand the processes determining the surface air warming over TP, raw outputs on model coordinates provided by ERA-5 and JRA-55 are used to diagnose near surface air temperature change over a complex terrain. The near surface air temperature anomaly is governed by the thermodynamic equation which is written at the lowest terrain-following model level as:

$$\frac{\partial T'}{\partial t} = -\vec{\boldsymbol{V}}' \cdot \nabla \bar{T} - \overline{\vec{\boldsymbol{V}}} \cdot \nabla T' - (\vec{\boldsymbol{V}}' \cdot \nabla T')' - (\dot{\eta}\frac{\partial T}{\partial \eta})' + (\frac{\kappa T \omega}{p})' + Q'_d, \quad (1)$$

where T, $\vec{V}$, and ω indicate the temperature, the horizontal wind, and the vertical velocity, respectively. η denotes the hybrid sigma-pressure vertical coordinate and $\dot{\eta} = d\eta/dt$. p denotes the pressure. κ is the ratio between the specific heat capacity of air and dry-air gas constant. Q_d is the diabatic heating which is generated by the model used to produce the reanalysis, including the longwave and shortwave radiative heating, vertical diffusion heating and latent heat release. The overbar indicates the climatological mean and the prime the departure from the climatological mean. The first two terms on the right-hand side of Eq. (1) are the anomalous horizontal temperature advections by the anomalous wind and the anomalous temperature, respectively. The third term indicates the nonlinear temperature advection anomaly by the anomalous wind and temperature. The fourth term is the anomalous vertical temperature advection. The fifth term denotes the adiabatic heating anomaly and the last term is the diabatic heat anomaly.

Different from the near surface air temperature which is primarily driven by combination of advection and local diabatic heating, GST is fundamentally determined by the radiative and turbulent eddy mixing processes (Clark and Feldstein 2020), which can be diagnosed with surface energy balance relation:

$$S^{\downarrow} - S^{\uparrow} + F^{\downarrow} - F^{\uparrow} - SH^{\uparrow} - LH^{\uparrow} = Q_s^{\downarrow}, \tag{2}$$

where S (F) denotes the surface shortwave (longwave) radiation flux, SH (LH) the surface sensible (latent) heat flux, and $Q_s^{\downarrow}$ the heat storage by land surface which is almost invariable and confirmed by each reanalyses (figure not shown). The directions of those fluxes are indicated with upward or downward arrows. The downward shortwave radiation (DSR) anomalies are decomposed into changes in both surface albedo and a minute part of DSR following the method of Lu and Cai (2009). The surface sensible and latent heat flux anomalies are determined by the anomalies of atmospheric and surface states, which can be linearly decomposed into two components with one affected by the anomalies of temperature (humidity) difference between land and air and the other affected by the wind speed anomalies, following the method of Wang et al. (2018). The surface upward longwave radiation flux can be represented as $F^{\uparrow} = \varepsilon\sigma T_s^4$, where T_s represents GST and ε and σ the surface emissivity and Stephen Boltzmann constant, respectively. In terms of Eq. (2), the GST anomaly can be estimated with use of the approximation method proposed by Lu and Cai (2009) as:

$$\Delta T_s \approx (\Delta S^{\downarrow} - \Delta S^{\uparrow} + \Delta F^{\downarrow} - \Delta SH^{\uparrow} - \Delta LH^{\uparrow} - \Delta Q_s^{\downarrow})/4\varepsilon\sigma\bar{T}_s^3, \tag{3}$$

Eqs. (1) and (3) imply a thermodynamic coupling between underlying surface and atmosphere (Clark and Feldstein 2020; Xie et al. 2022). For instance, when the land surface warms faster than the near surface atmosphere due to increased surface net downward radiative flux, the enlarged temperature difference between surface and air tends to increase upward sensible flux and promote an increase of SAT.

The DLR consists of components forced by cloud and clear sky atmosphere. The DLR change under clear sky involves processes of anthropogenic emissions of GHGs and water vapor change. In terms to the power law relationship between DLR under clear sky and vertically integrated water vapor (IWV) ($F_{iwv}^{\downarrow} = 147.8 \times IWV^{0.26}$) (Rangwala et al. 2009; Ruckstuhl et al. 2007), the DLR anomaly for clear sky can be decomposed into two parts respectively due to atmospheric water vapor and anthropogenic GHGs. The total DLR anomaly is then expressed as:

$$\Delta F^{\downarrow} = \Delta F_{clr}{}^{\downarrow} + \Delta F_{cld}{}^{\downarrow} = \Delta F_{iwv}{}^{\downarrow} + \Delta F_{res}{}^{\downarrow} + \Delta F_{cld}{}^{\downarrow}, \qquad (4)$$

where $\Delta F_{res}{}^{\downarrow}$ denotes a residual DLR anomaly, as the effects of cloud and atmospheric water vapor are removed, which is expected to represent the DLR change due to the change of anthropogenic GHGs. IWV is defined as specific humidity vertically integrated from surface to 100hPa, $IWV = (\frac{1}{g}\int_{100}^{ps} q dp)$, and its tendency is determined by:

$$\frac{\partial IWV}{\partial t} = -\nabla \cdot \frac{1}{g}\int_{100}^{ps}(q\vec{V})dp + E - P, \qquad (5)$$

where q is the specific humidity, ps the surface pressure, E the evaporation, P the precipitation, and $\nabla \cdot \frac{1}{g}\int_{100}^{ps}(q\vec{V})dp$ the divergence of vertically integrated water vapor flux.

3. Features of accelerated wintertime TP warming

The six reanalyses used are compared to the CMA observations to identify a reliable long-term trend of SAT over TP. Figures 1a and b show the time series and linear trends of SAT anomalies averaged over TP. There are significant warming trends over TP in the datasets except for NCEP-2, and the most pronounced warming is observed by CMA (0.55 K/dec). The reanalyses underestimate the warming rate commonly. The trends in ERA-5 (0.42 K/dec) and CRA-40 (0.42 K/dec) are stronger than in JRA-55 (0.37 K/dec), ERA-I (0.36 K/dec), MERRA-2 (0.28 K/dec), and NCEP-2 (0.11 K/dec). ERA-5 and JRA-55 match the CMA observations in the temporal variation of SAT, while CRA-40 and ERA-I behavior slightly worse (Fig. 1b).

Reliabilities of SAT temporal variations in the reanalyses seem to be associated with the resolution of the model generating the reanalysis. The SAT in NCEP-2 with a relatively coarse model resolution shows the lowest correlation with the CMA observations (0.42), indicating the necessity of using fine model resolution reanalyses in investigating SAT change over TP.

In terms of spatial distribution, the magnitude of warming rate is not uniform among 80 CMA stations over TP. The median value of the warming rate for the CMA observations is 0.54 K/dec, and the 25th and 75th percentiles are 0.34 K/dec and 0.72 K/dec, respectively (Fig. 1c). ERA-5 and JRA-55 match better with the CMA observations than other reanalyses in quantile statistics. The warming rate for NCEP-2 varies greatly among stations with a median value of 0.07. In observation, there are three prominent warming centers, located over the central, south-eastern, and western TP (Fig. 1d). These warming centers are reproduced by ERA-5 and CRA-40 (Figs. 2a, b). In addition, ERA-5 and CRA-40 display significant warming trends over the south slope of TP where the elevation changes rapidly. JRA-55 exhibits a similar warming trend with observation over the central and eastern TP, but no significant warming is observed over the south-western slope (Fig. 2c). The largest warming center over the central TP is also captured in ERA-I but has not been reproduced by MERRA-2 (Figs. 2d, e). NCEP-2 is inconsistent with observation and even exhibits a significant cooling over the northeastern TP (Fig. 2f).

When intercomparisons are performed among reanalyses, ERA-5 and CRA-40 show similarities in spatial distributions of surface air warming, while the warming in JRA-55 resembles that in ERA-I, especially over the central and western TP. The differences between reanalyses suggest the importance of resolution of the model generating the reanalyses. Two reanalyses (ERA-5 and CRA-40) with relatively fine model resolutions (approximately 30km) reproduce similar warming trends in areas with rapidly changing elevations. NCEP-2 with the lowest model resolution (~280km) deviates greatly to other reanalyses in both long-term trend and temporal variability of

SAT. The cold biases of SAT in reanalyses were also documented by some previous studies. Yan et al. (2020b) suggests that these cold biases could be attributed to the elevation difference between reanalysis model and reality. JRA-55, ERA-I and MERRA can be partly corrected by elevation-temperature correlation, but NCEP-2 still has larger cold biases after the correction. No surface observations assimilated and sparse model resolution may account for the weakness of NCEP-2. High resolution of reanalysis model can reduce the elevation bias and obtain a more precise trend of SAT, which is prominent in ERA-5 and CRA-40. In addition, the accurate performance of CRA-40 can be attributed to assimilations of multiple data from conventional observations and satellite instruments over East Asia.

The SAT change over TP relates to the tropospheric temperature variability. Figure 3 shows the cross sections of trend of air temperature over TP in ERA-5, CRA-40 and JRA-55. The latitude-altitude sections display a barotropic triple pattern with two significant warming centers over TP and the Arctic, respectively, and a cooling center in between. The warming over TP extends from surface to upper troposphere, which is also captured by the longitude-altitude sections. The warming is greater over the upper troposphere, because of an anomalous anticyclone shifting eastward with the raising of altitude, which is discussed in section 4. Previous studies investigated such a meridional temperature structure with the warming over the Arctic and the cooling over Eurasia during wintertime from several perspectives such as the stationary wavetrain energy propagation excited by the Barents-Kara Sea ice loss, the potential vorticity view of the dynamics in the interior atmosphere or the changes of the Ural blocking (Duan et al. 2022; Jin et al. 2020; Jolly et al. 2021; Xie et al. 2022). The total column warming over TP extend this equivalent barotropic dipole pattern to the mid-high latitude of Asia. The three reanalyses show similarity in structure of warming except for the intensity of the cooling center.

As seen from above, ERA-5, CRA-40, and JRA-55 have overall good performances in reproducing observed wintertime TP warming in SAT. In particular, ERA-5 captures well various characteristics of the observed warming, including its regional mean temporal variation and spatial distribution. Therefore, the results from ERA-5 are emphasized in the next sections, while those from other two reanalyses (CRA-40 and JRA-55) are provided in a supplementary material.

4. Processes of warming trend in surface air temperature

In this section, the thermodynamic equation, i.e., Eq. (1), is used to diagnose what determine the SAT change over TP. Due to the data availability, the diagnosis is performed on the lowest terrain-following level (approximately 10m above the surface), of the reanalysis model which was run on a hybrid sigma-pressure vertical coordinate, only for ERA-5 and JRA-55. The consistency of air temperature trends at the lowest level of model and at 2m above the surface is confirmed. As expected, the trends of air temperature at the lowest model level resembles the 2m-SAT trends in spatial patterns for both ERA-5 (Fig. 4a and Fig. 2a) and JRA-55 (Fig. S1a and Fig. 2c), except over Qaidam Basin in the northeastern TP. Qaidam Basin has an average elevation of about 1000m, where the processes of the SAT change may be different from those over the main body of TP. Therefore, it is appropriate to diagnose temperature budget on the lowest model level to explore the processes of surface air warming.

There are significant warming trends at the lowest model level over the central and southern TP with three prominent warming centers (Fig. 4a), which are consistent with the observed and reanalyzed trends of SATs at 2m (Fig. 1d and Fig. 2a). For the sake of finding dominant processes for the warming trends, a pattern correlation coefficient (PCC) between the trends of temperature tendency due to each of the terms at the right-hand side of Eq. (1) and SAT over TP is calculated and listed in top left-hand corner of each panel in Figs. 4b-f. It is found that the anomalous diabatic heating (Fig. 4f, PCC is 0.48) and the anomalous temperature advection by anomalous wind (Fig. 4b, PCC is 0.40) are two dominant processes determining the SAT trend (Fig. 4a). The diabatic heating is enhanced over TP south of 35°N and Qaidam Basin, with three maximum areas over the southeast, central and southwest slope of TP (Fig. 4f), which consists with the warming trend. The enhancement of diabatic heating is due to the surface skin warming, which are examined in detail in the next section. An increase of the warm advection of the climatological temperature by anomalous wind tends to warm the central and southern TP (Fig. 4b), which also agrees with the trend of SAT. The anomalous temperature advection by anomalous temperature tends to reallocate warm air from the southern TP to the northern TP (Fig. 4c). The change of anomalous vertical temperature advection is very weak near the surface (Fig. 4d). The adiabatic term is negatively correlated with the trend of SAT (Fig. 4e), which can be recognized as a compensation of atmospheric warming.

The relative contributions of those processes determining surface air warming are then quantified. Since the most significant warming occurs over the southern TP, the regional means are calculated over TP south of 35°N. The diabatic heating is the most critical contributor to the surface air warming with a magnitude of 0.1K/day/dec. The secondary is the warm advection of climatological temperature by anomalous wind (0.04K/day/dec). The trend of adiabatic heating is negative, and no significant long-term trends are observed in the other two advection terms. Thus, only two factors contribute to the surface air warming, which are the diabatic heating and the warm advection by anomalous wind, accounting for 71% and 29% of the warming trend over TP, respectively. Overall, these two dominant processes determining the surface air warming revealed in ERA-5 exist in JRA-55 (Fig. S1). There are also minor differences between the two reanalyses. Firstly, spatial distributions of surface air warming in the two datasets are not exactly the same, as the warming in JRA-55 shifts to the central TP and the cooling is observed over the south slope of TP where the diabatic cooling occurs. Secondly, the anomalous warm advection occurs over the eastern TP in JRA-55 but over the western TP in ERA-5.

The warm advection by anomalous wind is driven by the atmospheric circulation change. Since the near surface circulation change is too complicated around TP, atmospheric circulation change at 500hPa is examined to seek reasons for temperature advection change. Figure 5 shows the spatial distributions of trends in geopotential height and horizontal wind at 200 and 500hPa in ERA-5, CRA-40 and JRA-55. There exist an anomalous anticyclone to the southeastern TP and an anomalous cyclone north of TP, which are coincident in the three reanalyses. The anomalous anticyclone strengthens southwesterlies, thus warming TP by increasing warm advection. The anticyclone shifts eastward slightly as the attitude reduces, resulting in a weak influence on the near surface air over TP. Previous studies suggest that the atmospheric circulation change around TP is related to a Rossby wavetrain originated from Barents-Kara Sea (Duan et al. 2022) and large-scale circulation changes in the midlatitudes (Smith et al. 2022; Sun et al. 2022).

The enhanced diabatic heating at the lowest model level is closely associated with the change in turbulent heat exchange between the underlying surface and the atmosphere. Figure 6 shows the trends of anomalous surface sensible heat flux and its two components, linearly determined by anomalous land-air temperature difference and anomalous wind speed, respectively. It is found that the enhanced diabatic heating (Fig. 4f) is quite consistent with the increased upward surface sensible fluxes in three reanalyses (left panels of Fig. 6). The increased upward sensible heat fluxes are caused primarily by the increased land-air temperature differences (middle panels of Fig. 6), rather than by the decreased wind speeds (right panels of Fig. 6). The increased land-air temperature differences are dominated by the increases of skin temperature, i.e., GST, as shown in Fig. 7a. As SAT is increasing over TP, GST is increasing in a larger magnitude than SAT over TP, indicating that GST plays an active role in warming the atmosphere over TP via sensible heating. The processes of the warming trend in GST are further investigated in the next section.

5. Processes of warming trend in skin temperature

In order to understand the causes of the warming trend in skin temperature, the surface energy balance relation, i.e., Eq. (3), is employed to diagnose what processes determine the warming. Figure 7 shows the spatial distributions of trends of GST and its components constrained by the surface energy balance in ERA-5. There is a strong surface warming occurring in the central and southern TP and Qaidam Basin (Fig. 7a), which is firstly associated with a decrease of the upward shortwave radiation (USR, Fig. 7c). By decomposing the USR anomaly into two components linearly determined by anomalous surface albedo and by anomalous DSR (Figs. 8a, b), it is found that the decreased USR is dominated by decreased surface albedo, which is further attributed to reduced snow water equivalent (SWE) (Fig. 8c). Thus, the reduction of SWE enlarges surface absorption of incident solar radiation, which tends to warm surface and forms a positive snow-albedo feedback in the accelerated surface warming. The warming effect of snow-albedo feedback over TP revealed in ERA-5 is also reproduced by both CRA-40 (Fig. 8d and Fig. S2c) and JRA-55 (Fig. 8e and Fig. S3c). The decreased SWE as seen from the reanalyses is confirmed by the CMA observation, in which 56 of 80 stations exhibit significantly consistent decreases of snow depth over TP (Fig. 8f).

Besides the snow-albedo feedback in the accelerated TP surface warming, the moist process feedback also involves in the warming. There exists an increase of DLR over TP, which tends to warm surface widely with maximums over the central-eastern TP and the southern slope of TP (Fig. 7d). The DLR anomaly is further decomposed into components in terms of Eq. (4), which are illustrated in Fig. 9. The increased DLR is partly due to the increase of atmospheric water vapor over TP (Fig. 9b and Fig. 10c), which is significant over the eastern TP and the southern slope of TP. The atmospheric wetting over TP has a magnitude of approximately two-thirds of that over the neighbouring oceans, contrasting to the drying over the continents around (Figs. 10a, b). Significant increases of IWV are found to be over the eastern TP (Fig. 10c). To examine processes of the atmospheric wetting, Figures 10d-f demonstrate the trends of terms in the vertically-integrated water vapor budget equation, i.e., Eq. (5). An intensified surface evaporation which tends to wet the atmosphere but an enhanced divergence of water vapor flux which tends to dry the atmosphere are found over the eastern TP (Figs. 10d, f). Although an enhanced convergence of vertically integrated water vapor flux occurs over Qaidam Basin and Bayankara Mountain, the overall trend of convergence of water vapor is negative over the eastern TP. Therefore, the significant atmospheric wetting over the eastern TP is primarily attributed to the enhancement of the surface evaporation. Such a process revealed in ERA-5 also exists in both CRA-40 and JRA-55, although the areas of wetting are not exactly the same among the reanalyses (Figs. S6 and S7). Thus, the moist process feedback in the accelerated TP surface warming works as follows. An initial surface warming tends to promote the surface evaporation and moisten the atmosphere aloft over the eastern TP, causing a further surface warming through increasing DLR.

It is noted that the surface evaporation change is largely constrained by the change in land-air humidity gradient. Since no surface humidity data is provided by reanalyses, here the land-air humidity gradient is replaced by the specific humidity difference between 2m and the lowest model level. The humidity difference between land and air increases over the eastern TP. As the surface humidity increase is larger than that of the air humidity over the eastern TP (Figs. 11a, b), the humidity difference between land and air increases over the eastern TP, indicating that the underlying surface plays an active role in wetting the atmosphere over TP through the evaporation. The increase of the surface humidity over the eastern TP is associated not only with the increase in skin temperature but also with the increase in soil moisture (Figs. 11c, d). Figure 12 shows the trends of factors which can modulate changes of soil moisture averaged over the eastern TP during four seasons. In spite of the reduced precipitation in winter, the soil moisture in winter increases evidently due to the increased precipitation in the preceding seasons. Thus, the increases of surface moisture play an essential role in the moist process feedback involving in the accelerated TP surface warming.

However, it is noted that the moist process feedback is only effective over the eastern TP. Over the western TP, there are two possible processes that may decrease the surface humidity and thus suppress the surface evaporation. Firstly, increases of surface temperature may not reach a threshold for ice/snow melt in the western TP where the climatological conditions are dry and cold (Fig. 13). Secondly, significant increases in lake numbers and areas owning to enhanced precipitation in the preceding seasons over the western TP (Lei et al. 2013; Zhang et al. 2020) may bring more ice surface and cut off evaporation in winter.

The other two components of anomalous DLR are associated with changes of cloud and anthropogenic emissions of GHGs. While the changes of cloud tend to cool the surface of TP (Fig. 9c), the anthropogenic emissions of GHGs contribute to the warming of the central and southern TP (Fig. 9d). In spite of bias in calculating anomalous DLR by GHGs as a residue in Eq. (4), it is plausible that the increases of DLR by the anthropogenic GHGs are larger over the surroundings than over TP, since the thickness of atmospheric column and thus the increases of GHGs are smaller over TP than over plains. The DLR changes contributed from each component are confirmed by CRA-40 and JRA-55 (Fig. S4 and Fig. S5), in which increased water vapor is still the primary driver for the enhancement of DLR over the eastern TP, and the anthropogenic GHGs mainly contribute to the surface warming over the southern TP.

In summary, the ground surface warming of TP is formed through three key processes, the snow-albedo feedback, the moist process feedback, and the increases of anthropogenic GHGs. These warming processes are balanced with the decreases of incident solar radiation (Fig. 7b) and the increases of upward turbulent heat fluxes (Figs. 7e, f) which result in the surface air warming. For quantifying each process, we average trends of GST and its components constrained by the surface energy balance over TP south of 35°N. The trend of GST induced by decreased USR is 0.29 K/dec. In the trend of GST induced by increased DLR, the increases of IWV and anthropogenic GHGs account for 0.18 K/dec and 0.15 K/dec, respectively. Therefore, the two local feedback processes, i.e., the snow-albedo and moist process feedbacks, explain 47% and 29% of the total surface warming, respectively, and the external forcing which is primarily driven by anthropogenic GHGs accounts for 24% of the surface warming. In addition, the surface warming over Qaidam Basin is driven primarily by increased DLR, instead of decreased USR.

6. Conclusions and discussion

The Tibetan Plateau has experienced an accelerated wintertime warming under global warming, but consensus on its causes has not yet been reached. To attribute and quantify external forcing and local feedback processes in the accelerated warming, we firstly investigate the long-term trends of changes in SAT with observational and reanalysis datasets. Based on high quality reanalyses we then examine this issue by diagnosing the surface air temperature budget and surface energy balance. To identify the processes in the atmospheric water vapor change, the moisture budget analysis is performed. The overall processes for the accelerated wintertime TP warming are illustrated in a schematic diagram (Fig. 14), and major findings are summarized as follows.

Significant surface air warming over TP is observed in CMA station records with three pronounced warming centers located over the central, southeastern and western TP. All the six reanalyses underestimate the warming rate, but ERA-5, CRA-40, and JRA-55 have overall good performances in reproducing observed warming in SAT, compared with ERA-I, MERRA-2 and NCEP-2, which may be associated with the relatively high resolution of the model generating the reanalysis, as well as the multiple data sources assimilated.

Enhanced diabatic heating (71%) and increased warm advection by anomalous southwesterlies (29%) are two major processes determining the surface air warming. The enhancement of diabatic heating is consistent with the increased upward surface sensible heat fluxes. The increased sensible heat fluxes are caused primarily by the increased land-air temperature differences which is dominated by the increases of GST. As SAT is increasing over TP, GST is increasing in a larger magnitude than SAT, indicating that GST plays a driving role in warming the atmosphere over TP. The increased warm advection is induced by an anomalous anticyclone southeast of TP, resulting from the large-scale atmospheric circulation changes.

The warming of land surface is attributed to increased surface absorption of radiation fluxes through three radiative processes. The external forcing is primarily due to increased emissions of anthropogenic GHGs which contributes to the warming by 24% through increasing downward longwave radiation. Two types of the local positive feedbacks which are triggered by the land surface warming are found to contribute to most of the warming. The declines of upward shortwave radiation coincide with decreased snow water equivalent over the prominent warming areas of TP. The reduced snow water equivalent increases surface absorption of incident solar radiation, which tends to warm the surface and form a positive snow-albedo feedback, accounting for 47% of the surface warming. The increases of downward longwave radiation are also driven by the atmospheric wetting over the eastern TP. The surface warming, which works with the increased soil moisture due to increased precipitation in the preceding seasons, tends to increase land-air humidity differences and promote surface evaporation to moisten the atmosphere aloft. The atmospheric wetting strengthens the downward longwave radiation and causes a further surface warming, and thus forms a moist process feedback, accounting for 29% of the surface warming. However, the moist process feedback is only effective over the eastern TP, as the climatological conditions of the underlying surface are dry and cold and the frozen lakes are expanded during winter in the western TP.

This study provides a systematic view on the accelerated wintertime TP warming in recent decades. The diagnoses imply that the warming is driven not only by the external forcing of TP such as the large scale atmospheric circulation change and the anthropogenic emissions of GHGs, but also by the local positive feedback processes. Predictably, the accelerated warming over TP will persist as the local positive feedback processes continue to exist in future. Climate model simulations also suggest amplified warming of TP in cold seasons under warming scenarios, which is likely related to increased anthropogenic forcing (Kang et al. 2019; Qu et al. 2020; Wang et al. 2019; Wu et al. 2022; You et al. 2019; Zhang et al. 2022). However, our study indicates that changes of atmospheric circulation contribute nearly one-third of the accelerated warming over TP in recent decades, but the anomalous circulation pattern features strong internal climate variability. So, there are still large uncertainties in whether the warming amplification will exist, or the warming can persist over TP in the coming decades.

In addition, due to the large capacity of heat and moisture storages in ocean, the accelerated TP warming is slightly weaker than the Arctic Amplification, which is a noticeable phenomenon under global warming. There are some similarities in the processes involving in the surface warming of the two “poles”, such as in moist process feedback (Sang et al. 2022). This may raise an issue on the connection between TP and Arctic in amplified warming. This has been noticed in recent studies (Bi et al. 2022; Duan et al. 2022; Zhang et al. 2019), but final conclusion has not yet been reached. On the other hand, the amplified Arctic and TP warming can significantly affect large scale atmospheric circulation over Eurasia (Jia et al. 2021; Li et al. 2020; Li et al. 2021; Liu et al. 2020; Lu et al. 2021; Yu et al. 2021). Important questions that we leave for future work are whether the two accelerated warming poles can interact with each other and what their combined climate effects are.

Declarations

Ethics approval and consent to participate

The authors follow the rules of good scientific practice.

Consent for publication

Written informed consent for publication was obtained from all participants.

Availability of data and material

The China Meteorological Administration (CMA) ground observation datasets and the CMA reanalysis project (CRA-40) are available from https://data.cma.cn. The fifth generation ECMWF reanalysis (ERA-5) and the ECMWF interim reanalysis (ERA-Interim) can be obtained from https://www.ecmwf.int/en/forecasts/datasets. The Japanese 55-year Reanalysis (JRA-55) and the NCEP-DOE Reanalysis 2 (NCEP-2) are available at https://rda.ucar.edu. The Modern-Era Retrospective Analysis for Research and Applications, version 2 (MERRA-2) is available at https://gmao.gsfc.nasa.gov/reanalysis/MERRA-2.

Competing interests

The authors have no relevant financial or non-financial interests to disclose.

Funding

This study is jointly supported by the National Key Basic Research and Development Program of China (2022YFE0106600) and the National Natural Science Foundation of China (41621005).

Authors' contributions

All authors contributed to the study conception and design. The main idea of the study was put forward by XQY. Material preparation, data collection and analysis were performed by MZ and XQY. The manuscript was written by MZ and improved by XQY. All authors reviewed and approved the final manuscript.

Acknowledgements

This study is jointly supported by the National Key Basic Research and Development Program of China (2022YFE0106600) and the National Natural Science Foundation of China (41621005).

REFERENCES

Bi M, Li Q, Yang S, Guo D, Shen X, Sun X (2022) Effects of Arctic sea ice in autumn on extreme cold events over the Tibetan Plateau in the following winter: possible mechanisms. Climate Dynamics 58:2281-2292. https://doi.org/10.1007/s00382-021-06007-0

Blackport R, Screen JA (2020) Insignificant effect of Arctic amplification on the amplitude of midlatitude atmospheric waves. Science advances 6:eaay2880. https://doi.org/10.1126/sciadv.aay2880

Cai D, You Q, Fraedrich K, Guan Y (2017) Spatiotemporal temperature variability over the Tibetan Plateau: altitudinal dependence associated with the global warming hiatus. Journal of Climate 30:969-984. https://doi.org/10.1175/JCLI-D-16-0343.1

Clark JP, Feldstein SB (2020) What drives the North Atlantic Oscillation's temperature anomaly pattern? Part I: The growth and decay of the surface air temperature anomalies. Journal of the Atmospheric Sciences 77:185-198. https://doi.org/10.1175/JAS-D-19-0027.1

Clark JP, Shenoy V, Feldstein SB, Lee S, Goss M (2021) The role of horizontal temperature advection in Arctic amplification. Journal of Climate 34:2957-2976. https://doi.org/10.1175/JCLI-D-19-0937.1

Dee DP et al. (2011) The ERA-Interim reanalysis: Configuration and performance of the data assimilation system. Quarterly Journal of the royal meteorological society 137:553-597. https://doi.org/10.1002/qj.828

Duan A, Liu S, Zhao Y, Gao K, Hu W (2018) Atmospheric heat source/sink dataset over the Tibetan Plateau based on satellite and routine meteorological observations. Big Earth Data 2:179-189. https://doi.org/10.1080/20964471.2018.1514143

Duan A et al. (2022) Sea ice loss of the Barents-Kara Sea enhances the winter warming over the Tibetan Plateau. npj Climate and Atmospheric Science 5:1-6. https://doi.org/10.1038/s41612-022-00245-7

Duan A, Wu G (2006) Change of cloud amount and the climate warming on the Tibetan Plateau. Geophysical Research Letters 33. https://doi.org/10.1029/2006GL027946

Duan A, Wu G, Zhang Q, Liu Y (2006) New proofs of the recent climate warming over the Tibetan Plateau as a result of the increasing greenhouse gases emissions. Chinese Science Bulletin 51:1396-1400. https://doi.org/10.1007/s11434-006-1396-6

Duan A, Xiao Z (2015) Does the climate warming hiatus exist over the Tibetan Plateau? Scientific reports 5:1-9. https://doi.org/10.1038/srep13711

Ebita A et al. (2011) The Japanese 55-year reanalysis "JRA-55": an interim report. Sola 7:149-152. https://doi.org/10.2151/sola.2011-038

Gao K, Duan A, Chen D, Wu G (2019) Surface energy budget diagnosis reveals possible mechanism for the different warming rate among Earth's three poles in recent decades. Science Bulletin 64:1140-1143. https://doi.org/10.1016/j.scib.2019.06.023

Gao Y, Li X, Leung LR, Chen D, Xu J (2015) Aridity changes in the Tibetan Plateau in a warming climate. Environmental Research Letters 10:034013. https://doi.org/10.1088/1748-9326/10/3/034013

Ghatak D, Sinsky E, Miller J (2014) Role of snow-albedo feedback in higher elevation warming over the Himalayas, Tibetan Plateau and Central Asia. Environmental Research Letters 9:114008. https://doi.org/10.1088/1748-9326/9/11/114008

Group MRIEW (2015) Elevation-dependent warming in mountain regions of the world vol 5. https://doi.org/10.1038/nclimate2563

Hersbach H et al. (2020) The ERA5 global reanalysis. Quarterly Journal of the Royal Meteorological Society 146:1999-2049. https://doi.org/10.1002/qj.3803

Jia X, Zhang C, Wu R, Qian Q (2021) Influence of Tibetan Plateau autumn snow cover on interannual variations in spring precipitation over southern China. Climate Dynamics 56:767-782. https://doi.org/10.1007/s00382-020-05497-8

Jin C, Wang B, Yang YM, Liu J (2020) "Warm Arctic-cold Siberia" as an internal mode instigated by North Atlantic warming. Geophysical Research Letters 47:e2019GL086248.

https://doi.org/10.1029/2019GL086248

Jolly E, D'andrea F, Rivière G, Fromang S (2021) Linking warm Arctic winters, Rossby waves, and cold spells: An idealized numerical study. Journal of the Atmospheric Sciences 78:2783-2799. https://doi.org/10.1175/JAS-D-20-0088.1

Kanamitsu M, Ebisuzaki W, Woollen J, Yang S-K, Hnilo J, Fiorino M, Potter G (2002) NCEP–DOE AMIP-II Reanalysis (R-2). Bulletin of the American Meteorological Society 83:1631-1644. https://doi.org/10.1175/BAMS-83-11-1631

Kang S et al. (2019) Linking atmospheric pollution to cryospheric change in the Third Pole region: current progress and future prospects. National Science Review 6:796-809. https://doi.org/10.1093/nsr/nwz031

Lei Y, Yao T, Bird BW, Yang K, Zhai J, Sheng Y (2013) Coherent lake growth on the central Tibetan Plateau since the 1970s: Characterization and attribution. Journal of Hydrology 483:61-67. https://doi.org/10.1016/j.jhydrol.2013.01.003

Li F, Wan X, Wang H, Orsolini YJ, Cong Z, Gao Y, Kang S (2020) Arctic sea-ice loss intensifies aerosol transport to the Tibetan Plateau. Nature Climate Change 10:1037-1044. https://doi.org/10.1038/s41558-020-0881-2

Li Q, Zhao M, Yang S, Shen X, Dong L, Liu Z (2021) A zonally-oriented teleconnection pattern induced by heating of the western Tibetan Plateau in boreal summer. Climate Dynamics:1-20. https://doi.org/10.1007/s00382-021-05841-6

Li Y, Su F, Tang Q, Gao H, Yan D, Peng H, Xiao S (2022) Contributions of moisture sources to precipitation in the major drainage basins in the Tibetan Plateau. Science China Earth Sciences 65:1088-1103. https://doi.org/10.1007/s11430-021-9890-6

Liu X, Chen B (2000) Climatic warming in the Tibetan Plateau during recent decades. International Journal of Climatology: A Journal of the Royal Meteorological Society 20:1729-1742

Liu Y, Lu M, Yang H, Duan A, He B, Yang S, Wu G (2020) Land–atmosphere–ocean coupling associated with the Tibetan Plateau and its climate impacts. National Science Review. https://doi.org/10.1093/nsr/nwaa011

Liu Z et al. CMA global reanalysis (CRA-40): Status and plans. In: Proc. 5th International Conference on Reanalysis, 2017. Nat. Meteor. Int. Canter Rome, Italy, pp 13-17.

Lu J, Cai M (2009) Seasonality of polar surface warming amplification in climate simulations. Geophysical Research Letters 36. https://doi.org/10.1029/2009GL040133

Lu M, Yang S, Wang J, Wu Y, Jia X (2021) Response of regional Asian summer monsoons to the effect of reduced surface albedo in different Tibetan Plateau domains in idealized model experiments. Journal of Climate 34:7023-7036. https://doi.org/10.1175/JCLI-D-20-0500.1

Meng F, Su F, Li Y, Tong K (2019) Changes in terrestrial water storage during 2003–2014 and possible causes in Tibetan Plateau. Journal of Geophysical Research: Atmospheres 124:2909-2931. https://doi.org/10.1029/2018JD029552

Niu T, Chen L, Zhou Z (2004) The characteristics of climate change over the Tibetan Plateau in the last 40 years and the detection of climatic jumps. Advances in Atmospheric Sciences 21:193-203. https://doi.org/10.1007/BF02915705

Pepin N, Deng H, Zhang H, Zhang F, Kang S, Yao T (2019) An examination of temperature trends at high elevations across the Tibetan Plateau: the use of MODIS LST to understand patterns of elevation-dependent warming. Journal of Geophysical Research: Atmospheres 124:5738-5756. https://doi.org/10.1029/2018JD029798

Qu X, Huang G, Zhu L (2019) The CO_2-induced sensible heat changes over the Tibetan Plateau from November to April. Climate Dynamics 53:5623-5635. https://doi.org/10.1007/s00382-019-04887-x

Qu X, Huang G, Zhu L (2020) CO_2-induced heat source changes over the Tibetan Plateau in boreal summer-Part I: the total effects of increased CO_2. Climate Dynamics 55:1793-1807. https://doi.org/10.1007/s00382-020-05353-9

Rangwala I, Miller JR, Xu M (2009) Warming in the Tibetan Plateau: possible influences of the changes in surface water vapor. Geophysical research letters 36. https://doi.org/10.1029/2009GL037245

Rangwala I, Sinsky E, Miller JR (2013) Amplified warming projections for high altitude regions of the northern hemisphere mid-latitudes from CMIP5 models. Environmental Research Letters 8:024040. https://doi.org/10.1088/1748-9326/8/2/024040

Ruckstuhl C, Philipona R, Morland J, Ohmura A (2007) Observed relationship between surface specific humidity, integrated water vapor, and longwave downward radiation at different altitudes. Journal of Geophysical Research: Atmospheres 112. https://doi.org/10.1029/2006JD007850

Sang X, Yang X-Q, Tao L, Fang J, Sun X (2022) Decadal changes of wintertime poleward heat and moisture transport associated with the amplified Arctic warming. Climate Dynamics 58:137-159. https://doi.org/10.1007/s00382-021-05894-7

Smith DM et al. (2022) Robust but weak winter atmospheric circulation response to future Arctic sea ice loss. Nature communications 13:1-15. https://doi.org/10.1038/s41467-022-28283-y

Sun X et al. (2022) Enhanced jet stream waviness induced by suppressed tropical Pacific convection during boreal summer. Nature communications 13:1-10. https://doi.org/10.1038/s41467-022-28911-7

Wang M et al. (2019) Recent recovery of the boreal spring sensible heating over the Tibetan Plateau will continue in CMIP6 future projections. Environmental Research Letters 14:124066. https://doi.org/10.1088/1748-9326/ab57a3

Wang T, Peng S, Lin X, Chang J (2013) Declining snow cover may affect spring phenological trend on the Tibetan Plateau. Proceedings of the National Academy of Sciences 110:E2854-E2855. https://doi.org/10.1073/pnas.1306157110

Wang T, Yang X-Q, Fang J, Sun X, Ren X (2018) Role of air–sea interaction in the 30–60-day boreal summer intraseasonal oscillation over the western North Pacific. Journal of Climate 31:1653-1680. https://doi.org/10.1175/JCLI-D-17-0109.1

Wang X, Chen D, Pang G, Ou T, Yang M, Wang M (2020) A climatology of surface–air temperature difference over the Tibetan Plateau: Results from multi-source reanalyses. International Journal of Climatology 40:6080-6094. https://doi.org/10.1002/joc.6568

Wang Z, Yang S, Luo H, Li J (2022) Drying tendency over the southern slope of the Tibetan Plateau in recent decades: role of a CGT-like atmospheric change. Climate Dynamics:1-13. https://doi.org/10.1007/s00382-022-06262-9

Wu G et al. (2015) Tibetan Plateau climate dynamics: recent research progress and outlook. National Science Review 2:100-116. https://doi.org/10.1093/nsr/nwu045

Wu Q, Li Q, Ding Y, Shen X, Zhao M, Zhu Y (2022) Asian summer monsoon responses to the change of land–sea thermodynamic contrast in a warming climate: CMIP6 projections. Advances in Climate Change Research 13:205-217. https://doi.org/10.1016/j.accre.2022.01.001

Wu Y, Yang S, Hu X, Wei W (2020) Process-based attribution of long-term surface warming over the Tibetan Plateau. International Journal of Climatology 40:6410-6422. https://doi.org/10.1002/joc.6589

Wu Y, Zheng H, Zhang B, Chen D, Lei L (2014) Long-term changes of lake level and water budget in the Nam Co Lake Basin, central Tibetan Plateau. Journal of Hydrometeorology 15:1312-1322. https://doi.org/10.1175/JHM-D-13-093.1

Xie Y, Wu G, Liu Y, Huang J, Nie H (2022) A dynamic and thermodynamic coupling view of the linkages between Eurasian cooling and Arctic warming. Climate Dynamics 58:2725-2744. https://doi.org/10.1007/s00382-021-06029-8

Xu W, Ma L, Ma M, Zhang H, Yuan W (2017) Spatial–temporal variability of snow cover and depth in the Qinghai–Tibetan Plateau. Journal of Climate 30:1521-1533. https://doi.org/10.1175/JCLI-D-15-0732.1

Yan H, Huang J, He Y, Liu Y, Wang T, Li J (2020a) Atmospheric water vapor budget and its long-term trend over the Tibetan Plateau. Journal of Geophysical Research: Atmospheres 125:e2020JD033297. https://doi.org/10.1029/2020JD033297

Yan L, Liu Z, Chen G, Kutzbach J, Liu X (2016) Mechanisms of elevation-dependent warming over the Tibetan plateau in quadrupled CO_2 experiments. Climatic Change 135:509-519. https://doi.org/10.1007/s10584-016-1599-z

Yan Y, You Q, Wu F, Pepin N, Kang S (2020b) Surface mean temperature from the observational stations and multiple reanalyses over the Tibetan Plateau. Climate Dynamics 55:2405-2419. https://doi.org/10.1007/s00382-020-05386-0

Yang K, Ye B, Zhou D, Wu B, Foken T, Qin J, Zhou Z (2011) Response of hydrological cycle to recent climate changes in the Tibetan Plateau. Climatic change 109:517-534. https://doi.org/10.1007/s10584-011-0099-4

Yao T et al. (2012) Different glacier status with atmospheric circulations in Tibetan Plateau and surroundings. Nature climate change 2:663-667. https://doi.org/10.1038/nclimate1580

Yao T et al. (2015) Multispherical interactions and their effects on the Tibetan Plateau's earth system: a review of the recent researches. National Science Review 2:468-488. https://doi.org/10.1093/nsr/nwv070

Yao T, Wu G, Xu B, Wang W, Gao J, An B (2019a) Asian water tower change and its impacts. Bulletin of Chinese Academy of Sciences (Chinese Version) 34:1203-1209. https://doi.org/10.16418/j.issn.1000-3045.2019.11.003

Yao T et al. (2019b) Recent third pole's rapid warming accompanies cryospheric melt and water cycle intensification and interactions between monsoon and environment: Multidisciplinary approach with observations, modeling, and analysis. Bulletin of the American Meteorological Society 100:423-444. https://doi.org/10.1175/BAMS-D-17-0057.1

You Q et al. (2021) Warming amplification over the Arctic Pole and Third Pole: Trends, mechanisms and consequences. Earth-Science Reviews 217:103625. https://doi.org/10.1016/j.earscirev.2021.103625

You Q, Fraedrich K, Ren G, Pepin N, Kang S (2013) Variability of temperature in the Tibetan Plateau based on homogenized surface stations and reanalysis data. International Journal of Climatology 33:1337-1347. https://doi.org/10.1002/joc.3512

You Q, Jiang Z, Moore G, Bao Y, Kong L, Kang S (2017) Revisiting the relationship between observed warming and surface pressure in the Tibetan Plateau. Journal of Climate 30:1721-1737. https://doi.org/10.1175/JCLI-D-15-0834.1

You Q, Kang S, Pepin N, Flügel W-A, Sanchez-Lorenzo A, Yan Y, Zhang Y (2010) Climate warming and associated changes in atmospheric circulation in the eastern and central Tibetan Plateau from a homogenized dataset. Global and Planetary Change 72:11-24. https://doi.org/10.1016/j.gloplacha.2010.04.003

You Q, Zhang Y, Xie X, Wu F (2019) Robust elevation dependency warming over the Tibetan Plateau under global warming of 1.5 °C and 2 °C. Climate Dynamics 53:2047-2060. https://doi.org/10.1007/s00382-019-04775-4

Yu W, Liu Y, Yang X, Wu G, He B, Li J, Bao Q (2021) Impact of North Atlantic SST and Tibetan Plateau forcing on seasonal transition of springtime South Asian monsoon circulation. Climate Dynamics 56:559-579. https://doi.org/10.1007/s00382-020-05491-0

Zhang G et al. (2020) Response of Tibetan Plateau lakes to climate change: Trends, patterns, and mechanisms. Earth-Science Reviews 208:103269. https://doi.org/10.1016/j.earscirev.2020.103269

Zhang J, You Q, Wu F, Cai Z, Pepin N (2022) The Warming of the Tibetan Plateau in Response to Transient and Stabilized 2.0° C/1.5° C Global Warming Targets. Advances in Atmospheric Sciences 39:1198-1206. https://doi.org/10.1007/s00376-022-1299-8

Zhang Y, Gao T, Kang S, Shangguan D, Luo X (2021) Albedo reduction as an important driver for glacier melting in Tibetan Plateau and its surrounding areas. Earth-Science Reviews 220:103735. https://doi.org/10.1016/j.earscirev.2021.103735

Zhang Y, Zou T, Xue Y (2019) An Arctic-Tibetan connection on subseasonal to seasonal time scale. Geophysical Research Letters 46:2790-2799. https://doi.org/10.1029/2018GL081476

Zhao B, Zhang B, Shi C, Liu J, Jiang L (2019) Comparison of the global energy cycle between Chinese reanalysis interim and ECMWF reanalysis. Journal of Meteorological Research 33:563-575. https://doi.org/10.1007/s13351-019-8129-7

Zhao Y, Zhou T (2020) Asian water tower evinced in total column water vapor: A comparison among multiple satellite and reanalysis data sets. Climate Dynamics 54:231-245. https://doi.org/10.1007/s00382-019-04999-4

Zhou C, Wang K (2017) Contrasting daytime and nighttime precipitation variability between observations and eight reanalysis products from 1979 to 2014 in China. Journal of Climate 30:6443-6464. https://doi.org/10.1175/JCLI-D-16-0702.1

Table 1. Detailed information of six reanalysis datasets used in the study.

Dataset name	Horizonal resolution	Vertical resolution	Assimilation algorithm
ERA-5	T639 (31km)	137 hybrid level	4DVar
CRA-40	T574 (34km)	64 hybrid level	3DVar
JRA-55	T319 (60km)	60 hybrid level	4DVar
ERA-Interim	T255 (80km)	60 hybrid level	4DVar
MERRA-2	0.5×0.625 (50km)	72 hybrid level	3DVar
NCEP-DOE	T62 (210km)	28 sigma level	3DVar

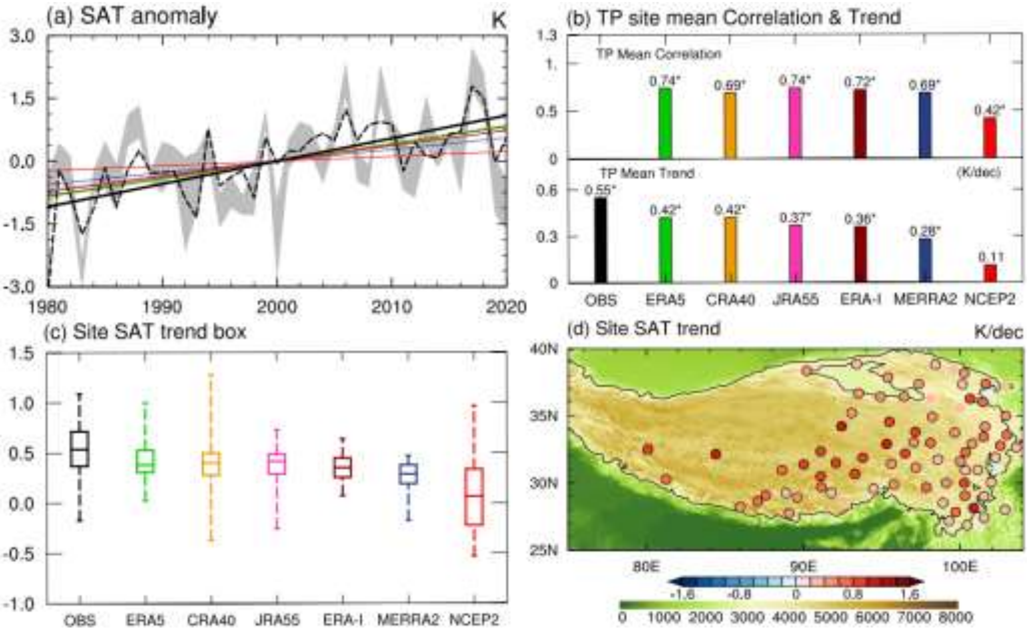

Figure 1. Intercomparison among CMA station observations and six reanalysis datasets in wintertime SAT anomalies. (a) Temporal variations (K) and linear trends (K/dec) of 80-station averaged SAT anomalies during 1980-2020, in which the black dashed line represents the CMA observations, the grey shading the range of six reanalyses, and the solid lines the linear trends of the datasets. (b) Temporal correlation coefficients between CMA observations and six reanalyses, and linear trends (K/dec) of SAT anomalies for all the seven datasets. (c) Statistical distributions of linear trends (K/dec) of SAT anomalies among 80 CMA stations. (d) Horizontal distribution of linear trends of the SAT anomalies for CMA observations (dots; K/dec) and elevation (shading; m), in which the black circles of stations denote SAT trends with the confidence level exceeding 95%, and the black curve outlines the TP areas with an averaged altitude higher than 3000m.

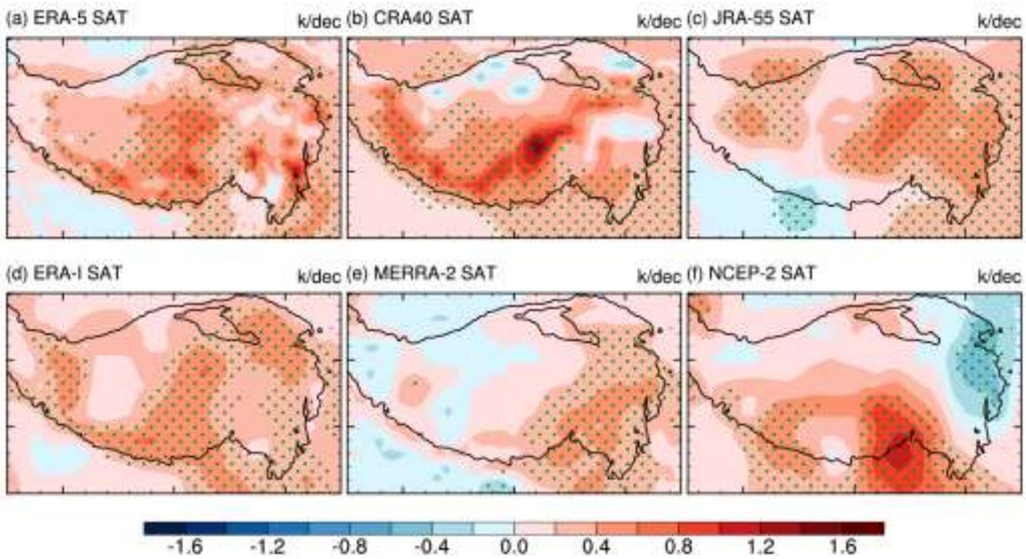

Figure 2. Horizontal distributions of linear trends of wintertime SAT anomalies (K/dec) at 2m for (a) ERA-5, (b) CRA-40, (c) JRA-55, (d) ERA-I, (e) MERRA-2, and (f) NCEP-2. The green dots denote the trends with the confidence level exceeding 95%. The black curve outlines the TP areas with an averaged altitude higher than 3000m.

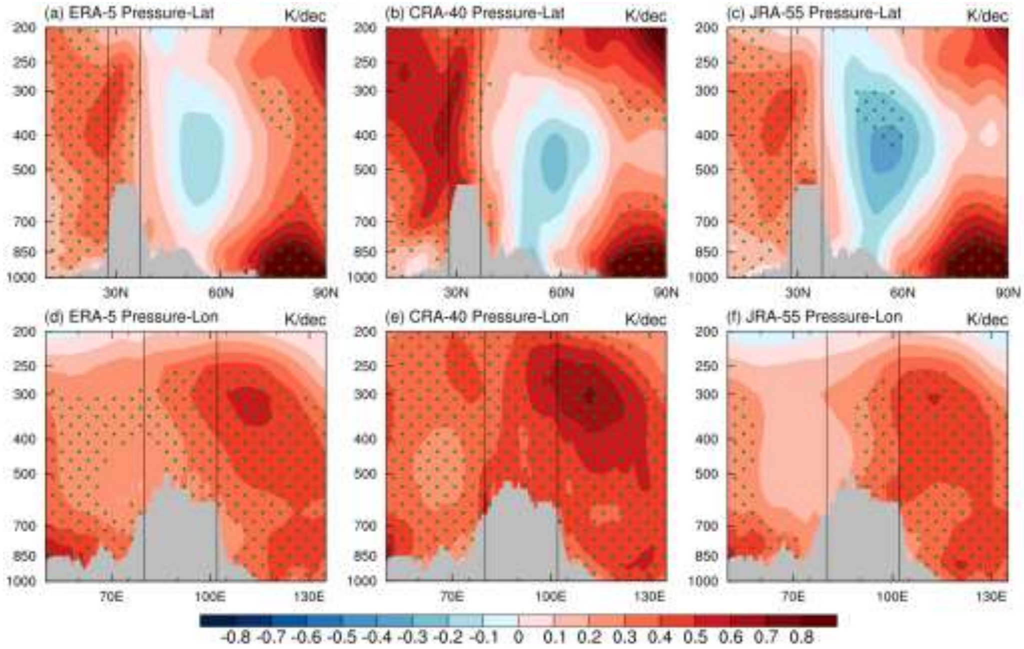

Figure 3. Latitude-altitude (top panels) and longitude-altitude (bottom panels) sections of linear trends of the air temperature (K/dec) averaged over TP for ERA-5 (left panels), CRA-40 (middle panels), and JRA-55 (right panels). The green dots denote the trends with the confidence level exceeding 95%. The black rectangle areas represent the TP regions.

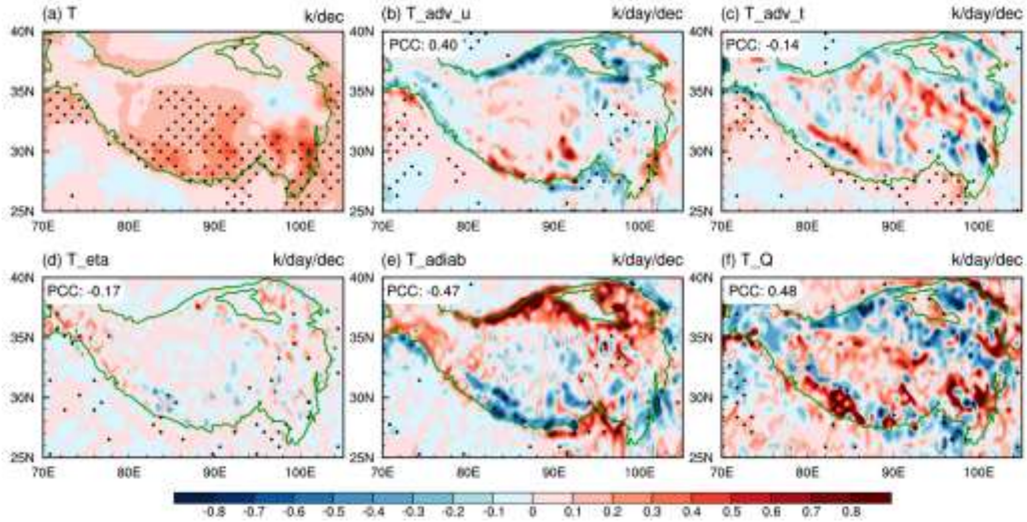

Figure 4. Horizontal distributions of linear trends of (a) the temperature (K/dec) and its budget anomalies (K/day/dec) for (b) horizontal advection of climatological temperature by anomalous wind, (c) horizontal advection of climatological wind by anomalous temperature, (d) vertical temperature advection, (e) adiabatic heating, and (f) diabatic heating on the lowest model level for ERA-5. The black dots denote the trends with the confidence level exceeding 95%. The green curve outlines the TP areas with an averaged altitude higher than 3000m.

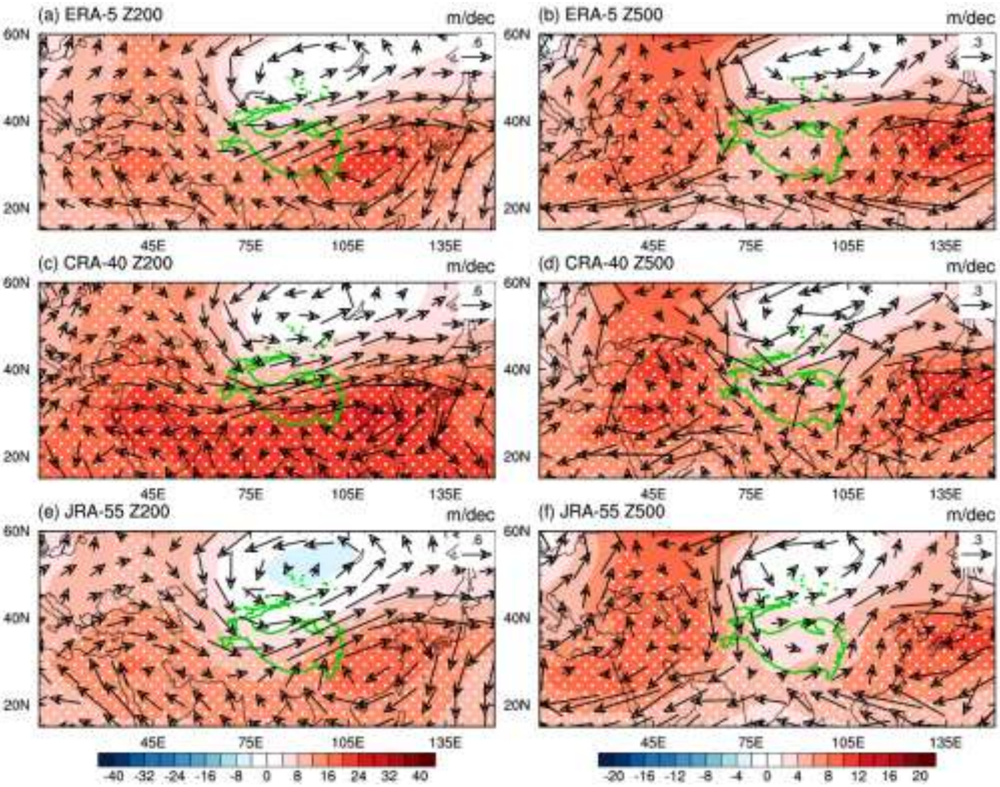

Figure 5. Horizontal distributions of linear trends of the 200 hPa (left panels) and 500 hPa (right panels) geopotential height (shading; m/dec) and horizontal wind (vector; m/s/dec) anomalies for ERA-5 (top panels), CRA-40 (middle panels), and JRA-55 (bottom panels). The white dots denote the trends of geopotential height with the confidence level exceeding 95%. The green curve outlines the TP areas with an averaged altitude higher than 3000m.

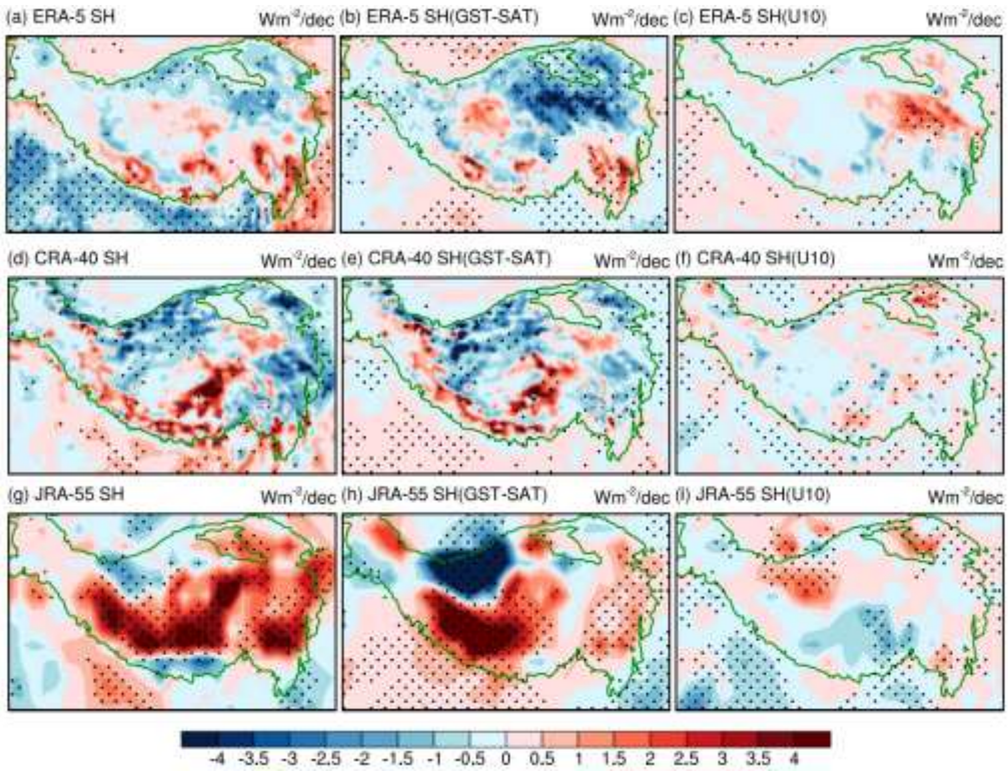

Figure 6. Horizontal distributions of linear trends of (a-c) the sensible heat flux anomalies (Wm^{-2}/dec, left panels) and their linear components due to (d-f) land-air temperature difference anomalies (middle panels), and (g-i) wind speed anomalies (right panels) for ERA-5 (top panels), CRA-40 (middle panels), and JRA-55 (bottom panels). The black dots denote the sensible heat flux aomalies with the confidence level exceeding 95%. The green curve outlines the TP areas with an averaged altitude higher than 3000m.

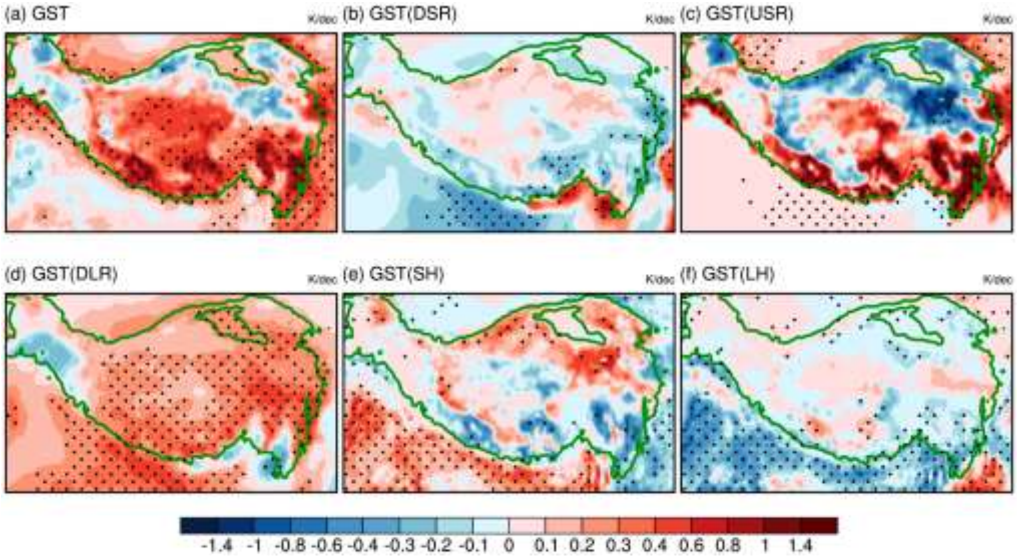

Figure 7. Horizontal distributions of linear trends of (a) the GST anomalies (K/dec) and its components constrained by the surface energy balance due to changes in (b) downward shortwave radiation (DSR), (c) upward shortwave radiation (USR), (d) downward longwave radiation (DLR), (e) surface sensible heat flux (SH), and (f) surface latent heat flux (LH) for ERA-5. The black dots denote the anomalies with the confidence level exceeding 95%. The green curve outlines the TP areas with an averaged altitude higher than 3000m.

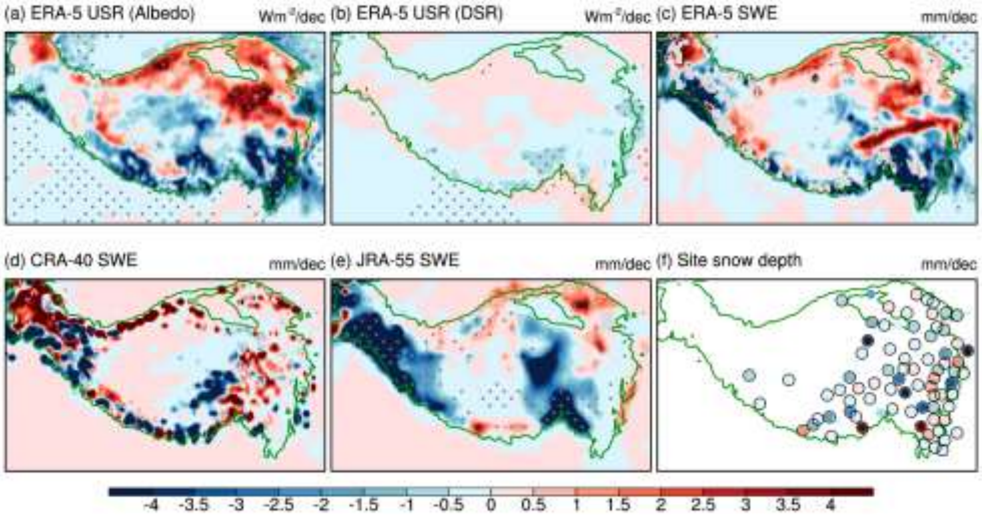

Figure 8. Horizontal distributions of linear trends of (a) the upward shortwave radiation (USR) anomalies induced by the albedo change (Wm^{-2}/dec) for ERA-5, (b) the upward shortwave radiation (USR) anomalies induced by the downward shortwave radiation (DSR) change (Wm^{-2}/dec) for ERA-5, the snow water equivalent anomalies (mm/dec, SWE) for (c) ERA-5, (d) CRA-40, and (e) JRA-55, and (f) the snow depth anomalies (mm/dec) for CMA station observations. The black dots in (a-e) and the black circles in (f) indicate the anomalies with the confidence level exceeding 95%. The green curve outlines the TP areas with an averaged altitude higher than 3000m.

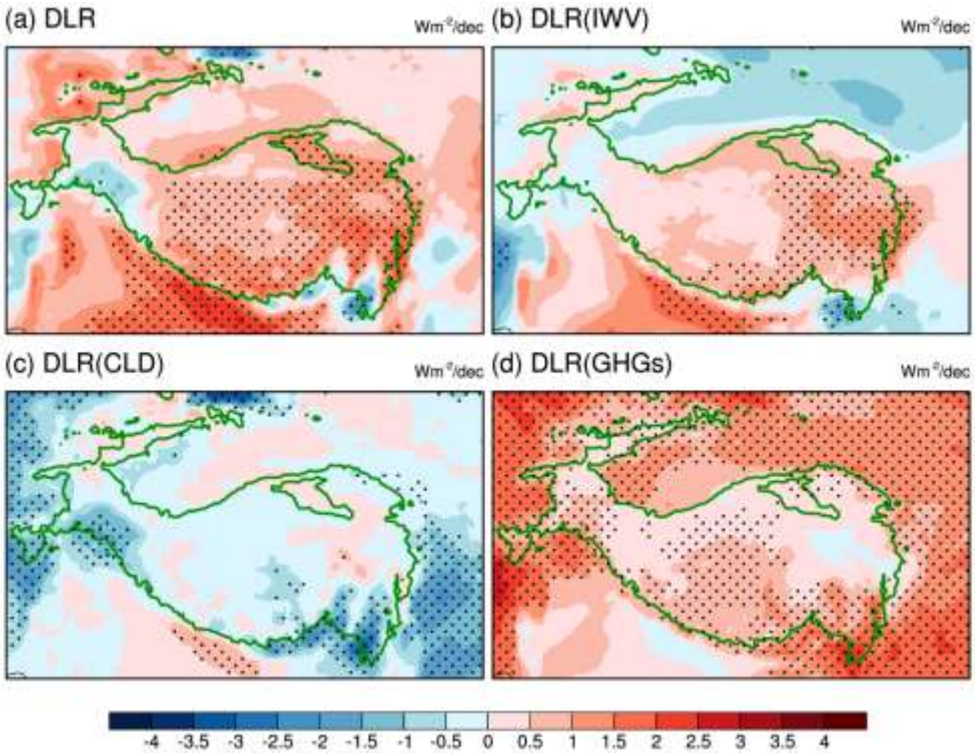

843

844 **Figure 9.** Horizontal distributions of linear trends of (a) the downward longwave
845 radiation (DLR) flux anomalies (Wm^{-2}/dec) and their components due to changes in (b)
846 atmospheric water vapor, (c) cloud, and (d) anthropogenic greenhouse gases for ERA-
847 5. The black dots denote the anomalies with the confidence level exceeding 95%. The
848 green curve outlines the TP areas with an averaged altitude higher than 3000m.
849

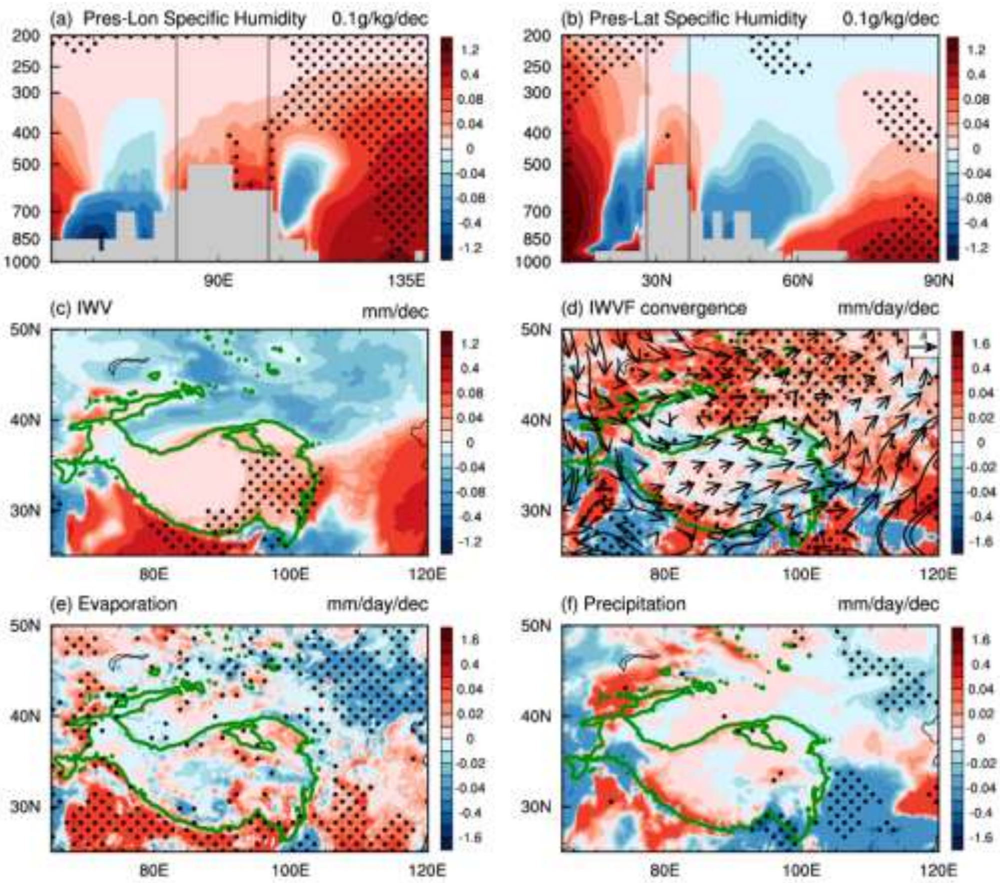

Figure 10. (a) Longitude-altitude and (b) latitude-altitude sections of linear trends of the specific humidity anomalies (0.1g/kg/dec) over TP for ERA-5. Horizontal distributions of linear trends of (c) the vertically integrated water vapor anomalies (mm/dec), (d) vertically integrated water vapor flux anomalies (vectors; kg/m/s/dec) and their convergences (shading; mm/day/dec), (e) the surface evaporation anomalies (mm/day/dec), and (f) the precipitation anomalies (mm/day/dec) for ERA-5. The black rectangle areas in (a) and (b) represent the TP region. The black dots denote the anomalies in shaded fields with the confidence level exceeding 95%. The green curve outlines the TP areas with an averaged altitude higher than 3000m.

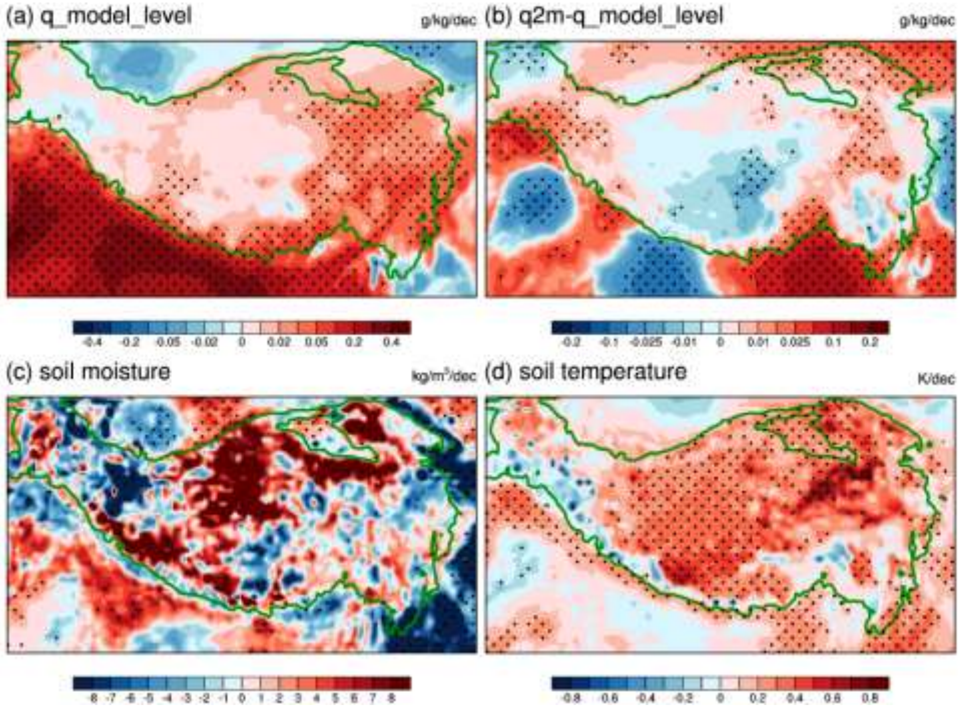

Figure 11. Horizontal distributions of linear trends of (a) the specific humidity anomalies (g/kg/dec) at the lowest model level, (b) the specific humidity difference anomalies (g/kg/dec) between 2m and the lowest model level, (c) the soil moisture anomalies (kg/m^3/dec), and (d) the soil temperature anomalies (K/dec). The black dots denote the anomalies in shaded fields with the confidence level exceeding 95%. The green curve outlines the TP areas with an averaged altitude higher than 3000m.

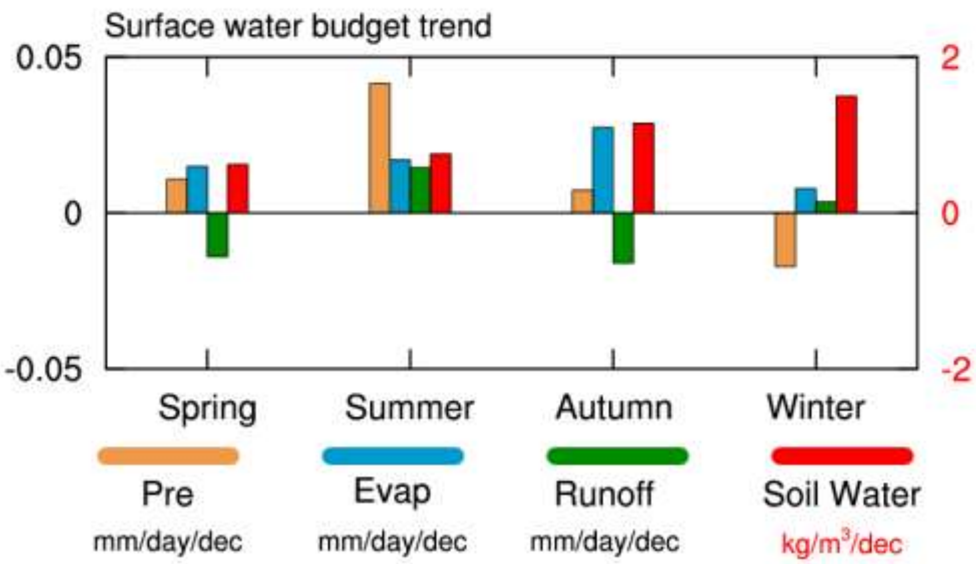

Figure 12. Linear trends of the precipitation (mm/day/dec), surface evaporation (mm/day/dec), runoff (mm/day/dec), and soil water (kg/m^3/dec) anomalies in four seasons averaged over the eastern TP (90-105°E, 26-40°N).

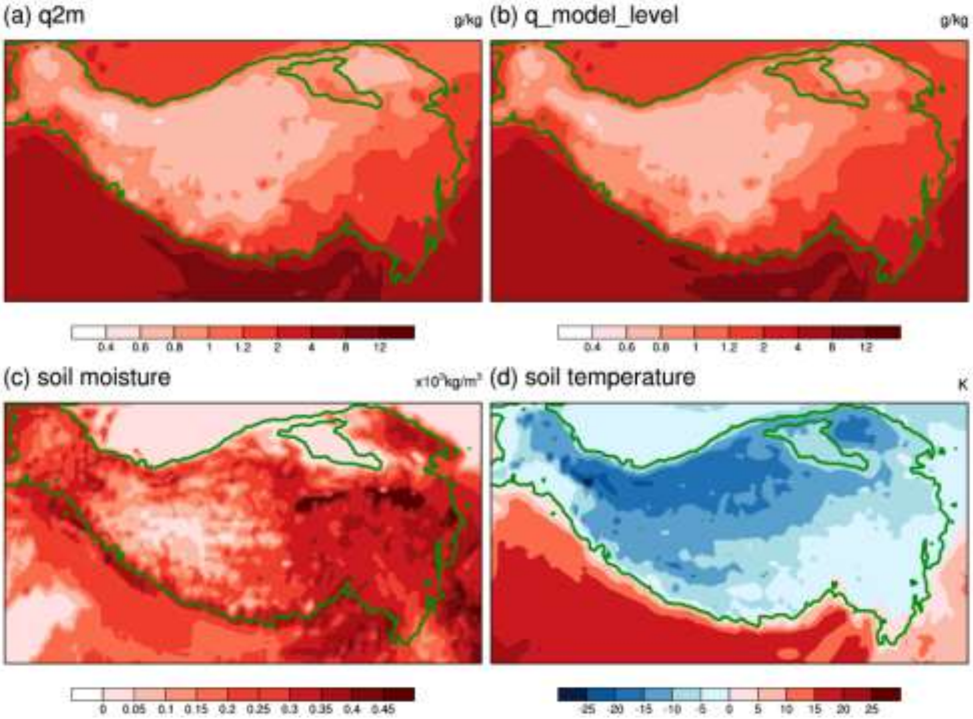

Figure 13. Horizontal distributions of the climatological specific humidity (g/kg) at (a) 2m above the surface and (b) the lowest model level, (c) soil moisture (10^3kg/m^3), and (d) soil temperature (K). The green curve outlines the TP areas with an averaged altitude higher than 3000m.

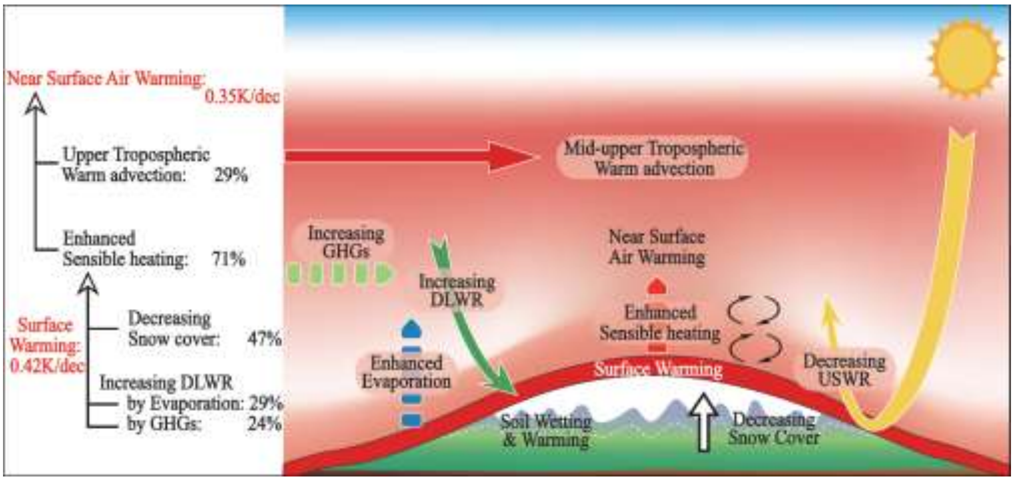

Figure 14. A schematic diagram for the quantified key processes involving in the accelerated wintertime TP warming.

Supplementary Files

This is a list of supplementary files associated with this preprint. Click to download.

- Supplementaryv4.docx